Fiber-Coupled Microcavity Probe – A Novel Optical Biosensor for Near-Field Real-Time Monitoring of Biomolecular Interactions

Nichaluk Leartprapun[1], Zachary Ballard[1], and Jimmy Xu[1, 2]
[1]School of Engineering
Brown University
Providence, USA
[2]WCU Program
Seoul National University
Seoul, South Korea
e-mail: Nichaluk_Leartprapun@brown.edu, Zachary_Ballard@brown.edu, Jimmy_Xu@brown.edu

Abstract – **We report on a novel optical biosensor design for near-field sensing based on a fiber-coupled microcavity. The device operates on the bases of sensing in the evanescent near-field zone via the amplitude and phase modulation of the reflected interference patterns. The integrated probe design offers a low-cost, robust and easy-to-fabricate alternative for label-free real-time biosensing. The first generation, pre-optimization device has already demonstrated sensitivity in the range of 10^{-4} and 10^{-5} refractive index units and 40 nm per refractive index unit. We have also demonstrated the potential use of this device in specific binding assays or concentration analyses by monitoring in real-time the solution-phase self-assembly of 5 Å aminosilane monolayer from varying bulk concentration. The application of this device as a new platform for point-of-care calibration-free concentration analysis is promising.**

Keywords – biosensor, microprobe, microcavity, fiber-optics, real-time sensing, silanization.

I. INTRODUCTION

Despite the prospects that optical biosensors could make sensitive and accurate point-of-care diagnostics a reality, bringing the technologies out of the lab setting (optical table) and into scalable devices for field use remains a tremendous challenge to many existing state-of-the-art optical biosensor platforms. We previously contributed a work-in-progress report on a novel label-free optical biosensor with a probe structure that is low-cost, robust, easy-to-fabricate, and has the potential for in-vivo or in-situ sensing and probing of bio-environments in the field settings [1] [2].

Electromagnetic waves interact with biological matter in various ways ranging from transmission, reflection, absorption, scattering and tunneling [3]. Utilizing different modes of light interactions with biological matter, a wide variety of optical biosensor platforms have been developed that probe the bio-environment via its localized refractive indices without the need for fluorescent markers or dyes. Surface-Enhanced Raman Spectroscopy (SERS) sensors rely on the plasmonic enhancement of light absorption and scattering to detect minute differences in the morphology of the sensing surface [4]. The modulation of wave characteristics of light upon reflections at interfaces allow interferometric biosensors to monitor the refractive index of the samples [5]. Surface Plasmon Resonance (SPR) sensors, one of the sensing platforms that have seen the most commercial success, rely on the absence of reflection during the phenomenon of light coupling into a surface mode at a specific incident angle [6]. State-of-the-art SPR sensor modules have been able to resolve refractive index in the orders of 10^{-7} to 10^{-9} refractive index unit (RIU). Garnering increasing research interests recently, the Whispering Gallery Mode (WGM) sensors are able to detect a single molecule or nanoparticle by coupling light into optical microcavity resonators [7][8]. These optical biosensor platforms are label-free, allowing for a more elegant detection protocol. Many of them are also capable of real-time sensing, an ability crucial to cellular studies and drug discoveries [9][10].

Though many breakthroughs have been made in regard to detection sensitivity, translating these from the laboratory into a portable and robust micro-device has yet seen significant success [2]. Existing high sensitivity biosensor platforms often required precise controls of moving parts on the nano-scale. Furthermore, the extensive and involved micro and nanofabrication required during the fabrication processes of some of these platforms make them much too expensive for most practical uses. Fiber-optic based platforms with sub-micron sized dimensions prove to be one of the more promising technologies in regard to the practicality of the device due to their needle-like geometries [11]. Despite the functional advantages and published sensitivities around 10^{-4} to 10^{-7} RIU, optical fiber based platforms still remain several orders of magnitude less sensitive than other bio-sensing technologies such as Surface Plasmon Resonance sensors, Whispering Gallery Mode sensors, and interferometric sensors [12]. However, novel fiber-based platforms could increase the capacity for sensitivity and serve as a more robust and low-cost biosensor solution. A portable and highly sensitive in-vivo device could have immense impact in driving down the cost

of healthcare and guiding vaccine and medicinal distribution networks [13].

In this work, we present a novel optical biosensor with a probe structure that has the potential for in-vivo or in-situ sensing and probing of bio-environments in real-time. This simple, portable, micro-scale device can detect, via phase-shift and amplitude change of the device response, minute changes in its microcavity's immediate vicinity (evanescence near-field zone). It could be used in diagnostics by detecting the presence of bio-targets such as deoxyribonucleic acid (DNA) and many disease biomarkers. In addition, it could be a possible low-cost tool to aid in the understanding of specificity and affinity of specific binding pairs by extracting kinetic information from real-time analysis. The ability to derive kinetic data from real-time measurements also opens the possibility of using this device as an alternative low-cost platform for calibration-free concentration analysis (CFCA) in point-of-care diagnostics [14][15]. The device integrates several characteristic features of existing more complex platforms such as multiple non-normal reflections and optical coupling from waveguide to microcavities into a single probe structure. The micro-probe consists of a micro-cavity formed at, and optically coupled to the tip of an optical fiber, resulting in a compact, easy-to-fabricate, and bio-compatible design for refractive index sensing. Experiments for the first generation device, with non-optimized probe geometries, have yielded a limit of detection of 10^{-4} to 10^{-5} RIU with the phase shift of 40 nm/RIU.

This article will first describe the fabrication and structure of the fiber-coupled micro-cavity probe. Then, propose the working principles of the device and present the experimental validations of the proposed principles. Finally, the article will demonstrate experimentally the capability of the device in bulk refractive index sensing and real-time monitoring of biomolecular interactions within the evanescence near-field zone.

II. Device Description

The micro-probe is made by tapering hollow borosillicate tubes (1mm OD, .75 mm ID) down to tip diameters of 25-50 µm. The tapering was achieved using a Sutter Instrument P-2000 Micropipette Puller. A 20W Class IV CO_2 laser was used as the heating source while the borosilicate tube was pulled from both sides, as shown in Fig. 1. Custom programs were written for the pipette puller to achieve long and gradual tapers. The tapered tips were then melted with a gentle flame from standard butane lighter, whereupon the molten glass forms a solid glass spherical tip due to its surface tension. The symmetry of the spherical tips was maintained by constant spinning of the tips during the melting process. The total resulting structure consists of a finely tapered air cavity that extends into a solid glass spherical tip, as seen in Fig. 2. Then, standard SMF-28 telecom fibers were stripped, cleaved and inserted into this tapered cavity, eventually becoming wedged. The optical fiber remains stationary due to the cylindrical geometry of the tapered air cavity and fiber, and can be affixed upon its insertion point with simple epoxy. The range of spherical tip diameters tested so far were, but not limited to, 300-500 microns.

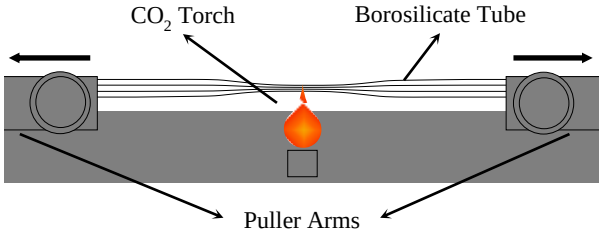

Figure 1. Borosilicate tube tapering process using a Micropipette Puller.

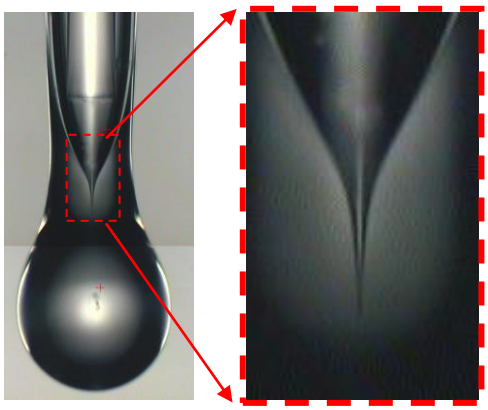

Figure 2. Device structure: Microscope image of SMF-28 fiber (125 µm diameter) wedged in tapered air cavity (red dotted outline) extending into glass spherical tip (410 µm diameter).

III. Working Principles

This section describes the working principles pf the fiber-coupled microcavity probe as a self-reference interferometer. Fizeau interferometry physics of the device is elaborated, followed by the discussion of its use as a sensor. Lastly, the experimental validations of the proposed working principles are presented.

A. *Fizeau Interferometry*

The resulting spherical probe structure contains two effective reflection surfaces for incident light through the optical fiber [16]. The first interface is between the end of the cleaved fiber and the air cavity, and the second interface is between the edge of the solid glass spherical tip and the outside environment, as shown in Fig. 3. Therefore, when incoming light through the fiber enters the device, the reflection from the second interface recombines with the reflection from the first interface as described by the reflection from an effective Fabry-Perot cavity.

The second interface is an effective one that is subjected to change by the material in the evanescence zone of the probe tip. The spherical tip forms a secondary (weak Q) cavity for the entering light scattered from the sharp air-tip.

Surrounding the outer surface of this microcavity is the aforementioned evanescence-zone. A change of material, temperature, humidity, or pH, even a minute one, in this zone would effectively change the size of this secondary cavity, which translates into the amplitude and phase modulation of the reflected light that can be measured from the overall interference pattern.

B. Use as a Sensor

Based on the Fizeau interferometer model, increasing the refractive index of the environment outside of the spherical tip naturally decreases the reflection coefficient for reflections below the critical angle and thus decreases the amplitude of the interference signal. However, this is not the only effect. Experiments show a clear phase change with changing refractive index in the exterior en vironments.

Due to the unique geometry of the sharply tapered air cavity between the two reflection interfaces, this device is able to bend the wave fronts of the fiber-outputted light. Fig. 4 illustrates the simulation of electric field and magnetic field intensity within the air cavity and the glass tip, showing the bent wave fronts as the electromagnetic wave escapes the tapered cavity. This bending of wave fronts allows for multiple reflections at multiple non-normal angles in the glass spherical tip and probe neck, eventually coupling the light back into the optical fiber. This light propagates in the spherical tip with a refractive index n_1 through a series of reflections with non-normal incident angle θ_i, where the reflections that meet the total internal reflection criteria are greatly affected by the Goos-Hänchen effect [17]. Changing the refractive index n_2 at the interface along the spherical tip will modulate the Goos-Hänchen shift, thus, shifting the interference pattern by a phase δ described by,

$$\tan\left(\frac{\delta_S}{2}\right) = \frac{\left(\sin\theta_i^{\,2} - n^2\right)^{\frac{1}{2}}}{\cos\theta_i} \qquad (1a)$$

$$\tan\left(\frac{\delta_P}{2}\right) = \frac{\left(\sin\theta_i^{\,2} - n^2\right)^{\frac{1}{2}}}{n\cos\theta_i} \qquad (1b)$$

where $n = n_2/n_1$.

Treating the device as an effective Fabry-Perot cavity [16], the total reflected intensity could be derived using the Airy Summation Method,

$$I_r(FP) = I_0\left[\frac{r_1^{\,2} + 2\cos(\delta)r_1r_2 + r_2^{\,2}}{1 + 2\cos(\delta)r_1r_2 + r_1^{\,2}r_2^{\,2}}\right] \qquad (2)$$

where r_1 and r_2 represent the reflection coefficient of the two interfaces of an asymmetric Fabry-Perot cavity. Substituting $r_1 = -r_2$ into (2) would recover the standard equation for the reflection of a symmetric Fabry-Perot cavity.

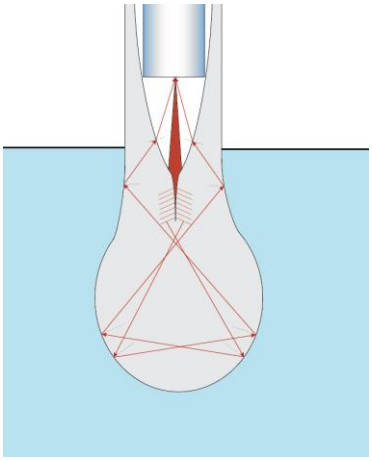

Figure 3. Ray-optics of light propagation in probe geometry.

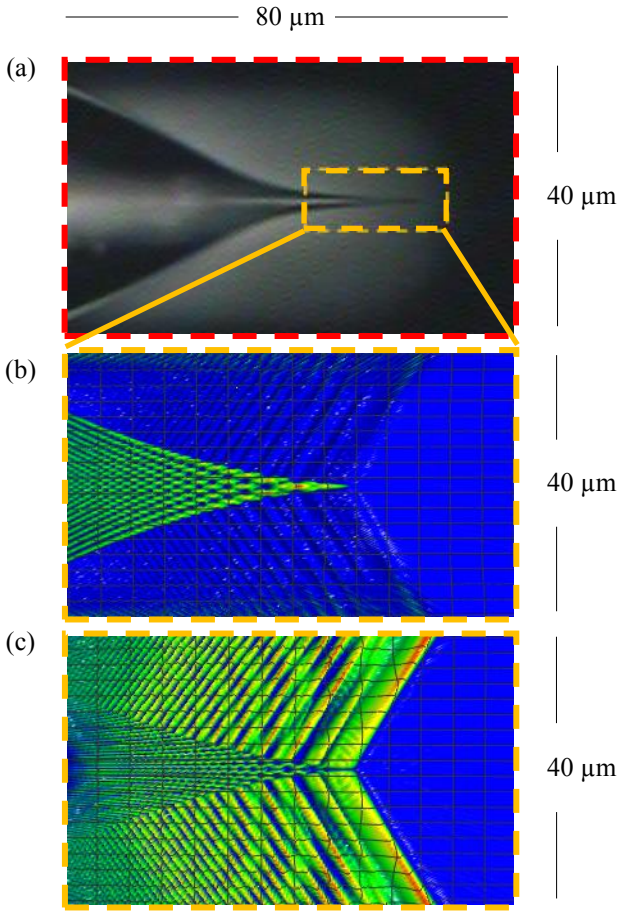

Figure 4. Tapered air cavity: (a) Microscope image of tapered cavity and Optiwave simulation of (b) electric field and (c) magnetic field intensity of light entering and escaping from the cavity.

To examine the effects of reflection angles on the output of the effective Fabry-Perot cavity model, (2) is used to simulate the interference patterns of the reflected signal in three cases: 1) reflection occurs at an angle smaller than the critical angles, 2) reflection occurs at an angle larger than

the critical angles, and 3) reflection occurs at multiple angles both smaller than and larger than the critical angles. Fig. 5 shows the simulated interference patterns of the three cases for n_2 values ranging from 1.00 to 1.30, corresponding to the critical angles from 42 degrees to 60 degrees. When the incident angle θ_i is set to 20°, the only effect of increasing the refractive index n_2 is the decrease in peak-to-peak amplitude due to the lessening of reflection coefficients for reflection below the critical angles. Changing the incident angle to 70°, however, causes the increasing refractive index to lose its effect on the reflection coefficients because of the reflection above the critical angle. Instead, the phase shift towards larger wavelength is observed as a result of increasing optical tunneling into the outside environment. If multiple reflections occur at multiple angles below and above the critical angle, both effects are observed and the reflected light experiences amplitude and phase modulation simultaneously as a result of varying refractive index in the evanescence zone.

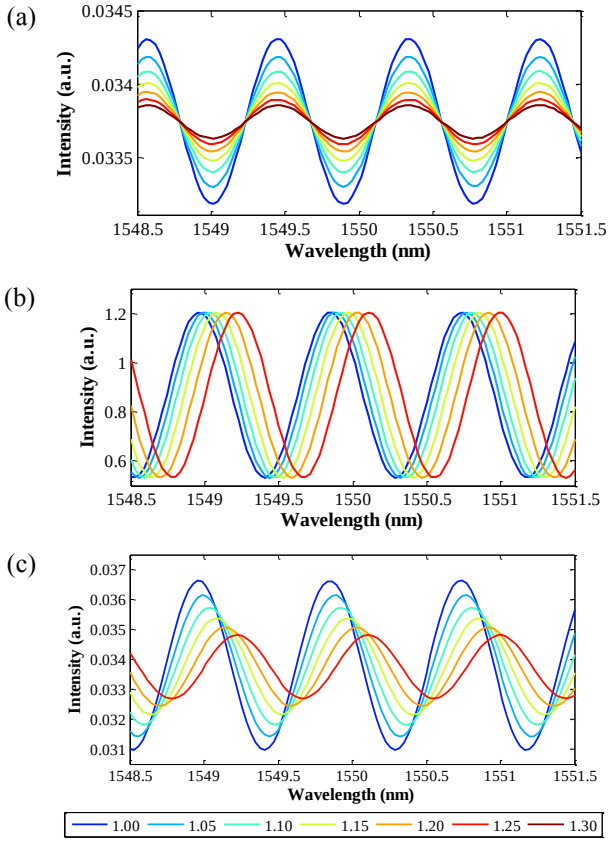

Figure 5. Simulation of interference patterns of reflected light: (a) reflection below critical angles only (θ_i = 20°), (b) reflection above critical angles only (θ_i = 70°) and (c) reflection both below and above critical angles (θ_i = 20° and θ_i = 70°).

C. *Experimental Validation of Working Principle*

To validate the model with the actual device output, Fig. 6 shows the model interference patterns produced from (2) for n_2 of air, water, and ethanol in comparison with the experimentally obtained results for the same environment in Fig. 7. The significant phase shift and amplitude decrease observed in the experimental results clearly indicate that multiple reflections at the incident angles both above and below the critical angles took place. This effective Fabry-Perot cavity model was able to describe the probe output remarkably well despite the complex structure and geometry of the device.

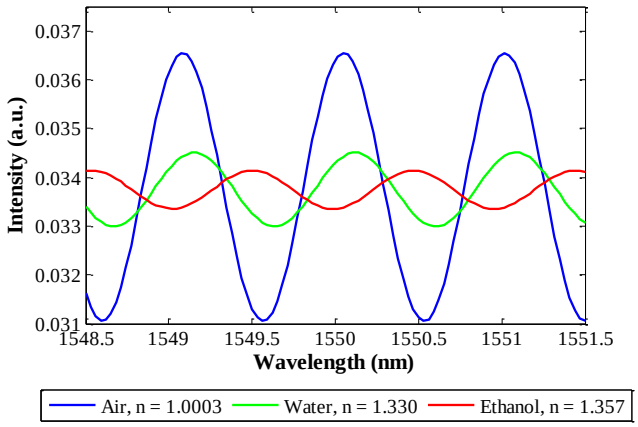

Figure 6. Output of probe model for outside refractive index environments of air, water, and ethanol.

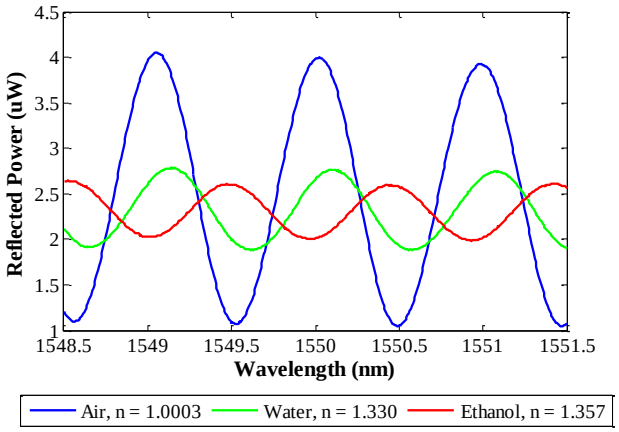

Figure 7. Reflected power (μW) measured for probe during 3 nm sweep in air, water, and ethanol.

The tapered air cavity, which gives rise to multiple reflections at multiple non-normal angles within the glass cavity, sets this fiber-coupled probe apart from conventional self-reference interferometers. The reflection above the critical angle provides an additional refractive index-sensitive effect, the Goos-Hänchen shift, unseen in devices with reflection only at normal angles.

IV. BULK REFRACTIVE INDEX SENSING

This section experimentally demonstrates the use of the fiber-coupled microcavity probe in bulk refractive index sensing. First, the experimental set-up for bulk refractive index measurements is described. Then, the bulk refractive index sensing performance is demonstrated with different volume fractions of ethanol and water mixtures.

A. *Experimental Set-Up*

The experimental set-up to demonstrate the interference properties of the fiber-coupled micro-sphere tip is illustrated in Fig. 8. An Ando AQ4320D Tunable Laser Source was wired to a 2×1 fiber optic coupler. The output of the coupler was sent to the SMF-28 fiber wedged in the micro-sphere tip. The reflected signal from the tip was measured by an Ando AQ6317 Optical Spectrum Analyzer wired to the second output of the coupler. Both the Tunable Laser Source and the Optical Spectrum Analyzer were connected to a PC and controlled by a LabVIEW VI. Spectra collection was also accomplished by the same program.

B. *Refractive Index Sensing with Ethanol-Water Mixture*

For a quantitative assessment of the sensitivity of this device, the probe was exposed to deionized water and then subsequently to incremental concentrations of ethanol-water mixtures ranging from 0 to 40% volume fraction of ethanol. The experiment was performed in a flow system so as to allow the injection of different mixtures without disturbing the probe or exposing it to contaminants that could be present in the air. In each mixture, a 3 nm spectral sweep was performed centered around 1550 nm with 1 mW laser power. The reflected power was measured and found to demonstrate a red spectral shift and a decrease in peak-to-peak amplitude with increasing ethanol concentration, as shown in Fig. 9. This result is in agreement with the model prediction when the refractive index of the immediate vicinity of the spherical tip, n_2, is increased.

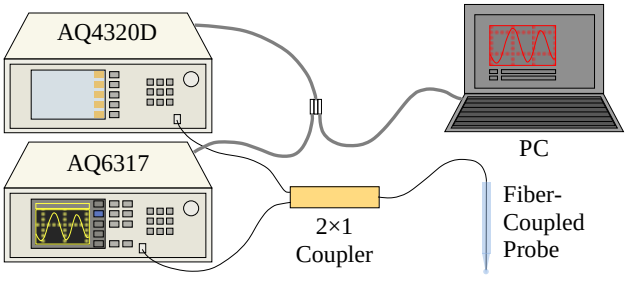

Figure 8. Experimental set-up for fiber-coupled micro-sphere tip interference measurements.

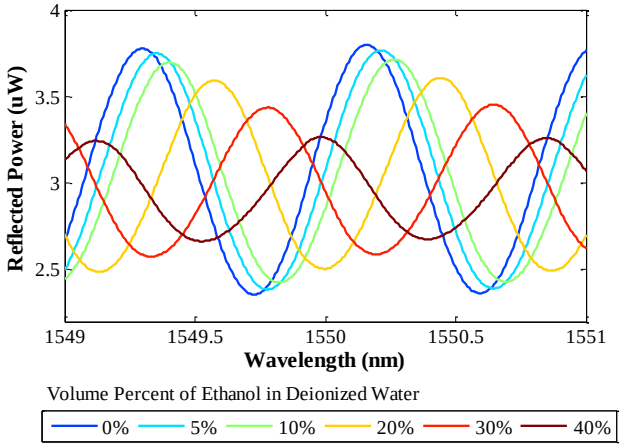

Figure 9. Red spectral shift and amplitude decrease of interference pattern as a result of exposure to 10^{-3} incremental changes in refractive index.

As a control, the second set of measurements was performed in the reverse order from higher to lower concentration of ethanol. The reflected signals were found to match those of the first set of measurements. The refractive index of each ethanol-water mixture was also measured using a Fisher Scientific Abbe Benchtop Refractometer. Fig. 10 plots the change in peak-to-peak amplitude of the spectrums and the shift in peak wavelength as a function of mixture refractive index. Both the amplitude and the phase of the spectrum exhibited a linear change with increasing refractive index. The device demonstrated the sensitivity in spectral shift of 40 nm/RIU.

The Limit of Detection (LOD) of the device was determined by performing the same measurements with smaller refractive index increments ranging from 0 to 2% ethanol volume fraction, as shown in Fig. 11. Although both the amplitude decrease and the red spectral shift were observed in the interference patterns, only the change in the peak-to-peak amplitude was resolvable by the Optical Spectrum Analyzer. Alternatively, when the amplitude change is small, the effect of the spectral shift can be magnified by measuring the reflected power at a single wavelength corresponding to the inflection point of the interference pattern. Fig. 12 plots the change in reflected power at the rising edge of the interference patterns, indicated by the dotted line in Fig. 11, and the change in peak-to-peak amplitude as a function of mixture refractive index. The device demonstrated the ability to detected minute changes in refractive index of the surrounding environment with the LOD in the range of 10^{-4} and 10^{-5} RIU. The optimization of the probe geometry such as the profile of the tapered air cavity could further enhance the LOD of the device.

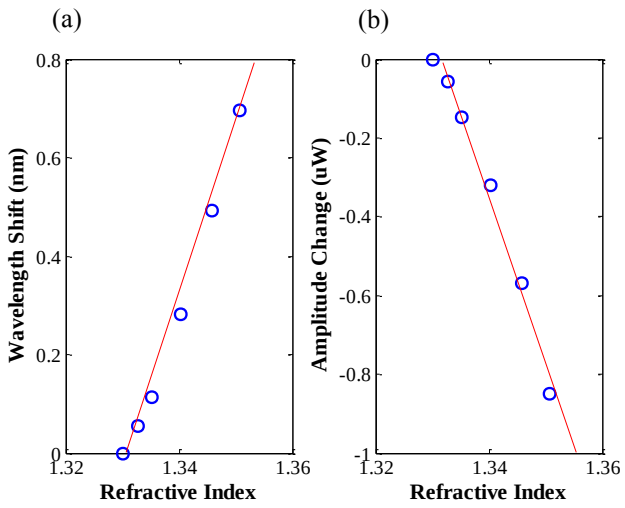

Figure 10. (a) Spectral shift, measured by the change in position of each interference peak, and (b) change in peak-to-peak amplitude of each interference pattern relative to 0% ethanol as a function of refractive index.

V. SURFACE BIOMOLECULAR INTERACTIONS SENSING

This section experimentally describes the use of the fiber-coupled microcavity probe in real-time monitoring of biomolecular interactions on the glass spherical tip. The experimental set-up described in Section IV applies. The reagents for the surface reactions and the experimental procedures are described, followed by the interpretation of the experimental results. Lastly, the proof-of-concept for the device application in concentration analysis is demonstrated.

A. Real-Time Monitoring of Silanization on Probe Tip

One of the advantages of optical biosensors such as the SPR sensors over other types of biosensors is the relative ease of performing real-time monitoring of cellular environments or specific binding events [18][19]. To demonstrate the biosensing capability of the microcavity probe, the formation of self-assembled monolayer of an aminosilane coupling agent was monitored in real-time. The probe surfaces were cleaned in Piranha solution (3:1 v/v of H_2SO_4:H_2O_2) and then placed in a solution of 2% v/v of 3-aminopropyltriethoxysilane (APTES) in acetone [20]. The solution was sealed with a molded polydimethylsiloxane (PDMS) stopper and polytetrafluoroethylene (PTFE) thread seal tape to avoid evaporation. The silanization of APTES refers to the deposition of APTES molecules onto an oxide substrate surface via hydrogen bonding, covalent bonding or electrostatic interactions. It is often used to functionalize inorganic silica substrates for selective binding of organic bio-targets [21]. The probe was incubated in the solution for 12 hours as continuous 3 nm spectral sweeps, centered around 1550 nm with 1 mW laser power, were taken. The interference patterns obtained during the 12-hour APTES silanization exhibit blue spectral shift, as shown in Fig. 13. The change in reflected power at a single wavelength corresponding to the dotted line is also plotted as a function of incubation time.

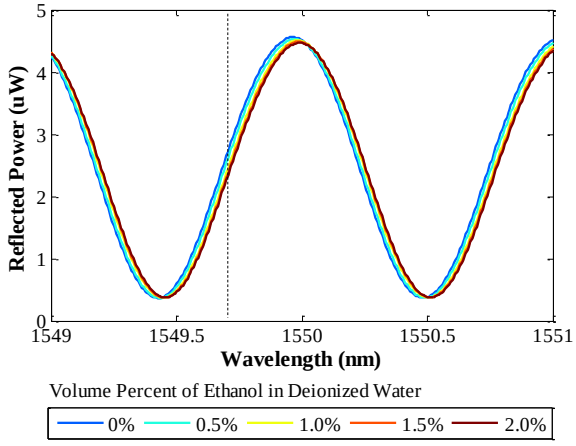

Figure 11. Red spectral shift and amplitude decrease of interference pattern as a result of exposure to 10^{-5} incremental changes in refractive index.

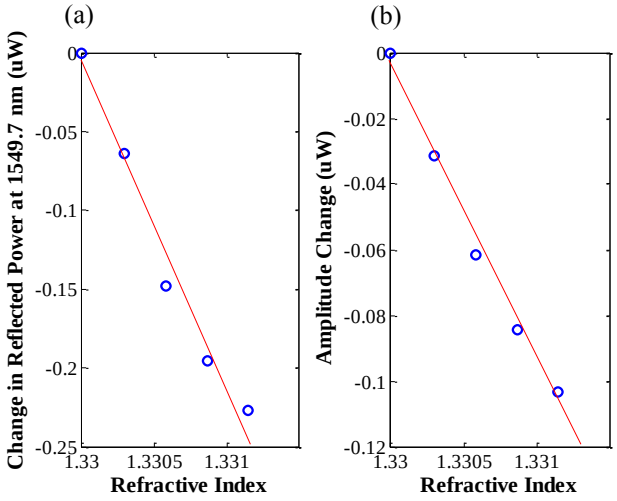

Figure 12. (a) Change in reflected power at 1549.7 nm, and (b) change in peak-to-peak amplitude of each interference pattern relative to 0% ethanol as a function of refractive index.

The change in reflected power at the rising edge illustrates the self-assembly of the APTES monolayer in the first 25-30 minutes, and subsequent intermolecular interactions of APTES molecules on top of this monolayer in the 12-hour period after the monolayer formation. The total spectral shift of approximately 0.2 nm was observed as a result. This observed monolayer binding time-scale (20-30 minutes) agrees with the standard protocol time-scale for a 5 Å monolayer deposition of APTES on a silica substrate from organic solvents [21].

B. Interpreting Blue Spectral Shift

It may be noted that the blue spectral shift as a result of molecular binding on the sensing surface is counter to the

red spectral shifts observed in typical resonance sensors, caused by an effective lengthening of the optical path due to the presence of the monolayer [22][23][24]. This counter-intuitive effect can be explained by the fundamentally different working principle of the fiber-coupled probe, which behaves like a self-reference interferometer, compared to those of the typical resonance sensors.

During the self-assembly of APTES molecules onto the spherical tip, the layer of surface-bounded molecules could be modeled as the third effective cavity, in addition to the air and the glass cavities discussed in Section III. The presence of this effective layer results in an additional effective reflection interface R_3 between the APTES layer and the bulk solution, as shown in Fig. 14. Thus, the total reflected signal is the product of the interference of three electromagnetic waves: $\mathbf{E_1}$, $\mathbf{E_2}$ and $\mathbf{E_3}$. The blue spectral shift could be caused by a lessening of optical tunneling into the bulk solution due to the higher refractive index difference $\Delta n = n_2 - n_3$ between the APTES layer and the bulk solution as more APTES molecules deposited onto the glass spherical tip.

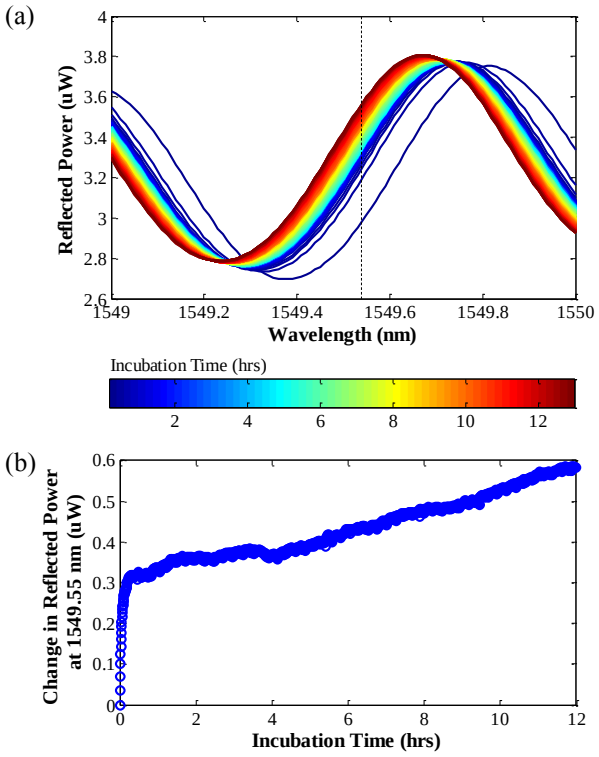

Figure 13. (a) Spectral shift of interference patterns and (b) change in reflected power at 1549.55 nm (dotted line in (a)) as a result of 12 hours incubation in APTES silanization solution.

Fig. 15 shows the predicted interference patterns during the self-assemble of APTES monolayer generated from (2), modified to include the third reflection surface. The refractive index and the thickness of the APTES monolayer were taken to be 1.46 and 5 Å, respectively [21]. The refractive index n_3 of the APTES in acetone solution was measured by the refractometer and assumed to remain constant during the 30 minutes incubation period. The refractive index n_2 was scaled from n_3, when the surface was free of APTES molecules, to 1.46, when the monolayer formation was completed, over the course of 30 minutes. The experimentally obtained interference patterns during the first 30 minutes of incubation in 2% v/v solution of APTES in acetone is also shown for comparison.

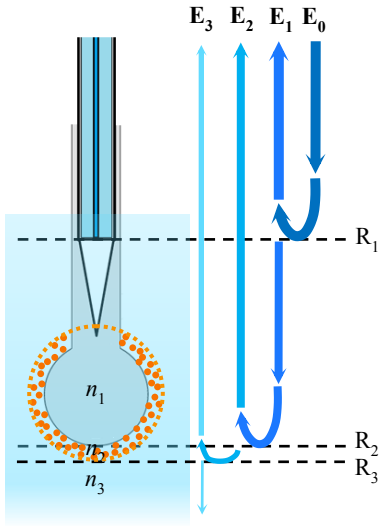

Figure 14. Light propagation in 3-layer Fabry-Perot cavity model with 3 reflection interfaces: R_1 between the cleaved end of the fiber and air, R_2 between the glass tip and surface-bounded molecules, and R_3 between the surface-bounded molecules and bulk environment.

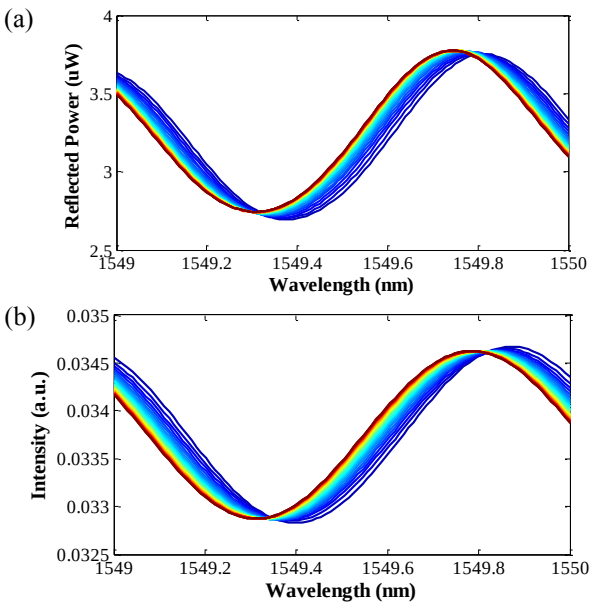

Figure 15. (a) Experimentally obtained spectral shift of interference patterns as a result of 30 minutes APTES monolayer formation and (b) model generated prediction of the same process.

The model successfully predicts the blue spectral shift of approximately the same magnitude as observed in the experimental results. Any discrepancies between the experimental results and the model prediction could be largely due to the distribution of model parameter n_2 over time, which could not perfectly replicate the actually refractive index modulations during the silanization process.

C. Concentration Analysis with Kinetic Data

The ability to perform real-time detection allows the biosensor to monitor the interactions of bio-targets with immobilized binding sites as they occur. Real-time biosensors such as the Biacore SPR modules are able to extract the kinetic constants of the given binding pair and subsequently determine the affinity and concentration of the target molecules [25][26]. To investigate the use of the fiber-coupled probe in concentration determination with kinetic data, the silanization of APTES performed at different bulk concentration ranging from 0.2 to 4% volume fraction of APTES in acetone were monitored. The probe was cleaned in Piranha solution prior to incubation in each silanization solution. The probe was incubated for 30 minutes in each solution, during which continuous 3 nm spectral sweeps, centered on 1550 nm with 1 mW laser power, were taken. The change in reflected power at a single wavelength corresponding to the rising edge of the interference patterns as a function of time is shown in Fig. 16. The change in reflected power was normalized to the value previously obtained from the 2% solution at the 30-minute mark, where the monolayer was assumed to have reached saturation.

The time profile of the normalized change in reflected power is fitted to the adsorption model based on the Langmuir-type physico-chemical reversible process [27]. The model consists of three Langmuir parameters: the adsorption capacity, Γ_{max}, defined as the ratio of the number of bounded molecules to the total number of binding sites at saturation, the association rate constant, k_a, and the dissociation rate constant, k_d; together they define both the reaction kinetics and the equilibrium adsorption isotherm of the process. Equation (3) describes the differential rate of adsorption based on the Langmuir adsorption model, where $\Gamma(t)$ is the time dependent ratio of number of bounded molecules to the total number of binding sites and C_0 describe the bulk concentration of the target molecules. The three Langmuir parameters were determined from the experimental data graphically as described in [27]. Solving (3) for $\Gamma(t)$, the model was fitted to the experimental data with C_0 as the only changing variable for different APTES concentrations.

$$\frac{d\Gamma(t)}{dt} = k_a C_0 \left(1 - \frac{\Gamma(t)}{\Gamma_{max}}\right) - k_d \Gamma(t) \qquad (3)$$

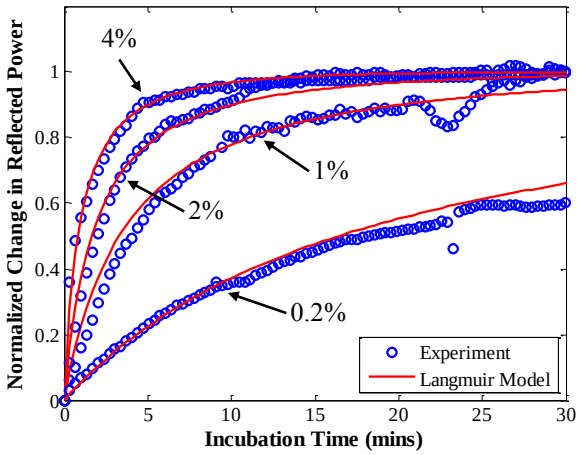

Figure 16. Experimentally obtained spectral shift of interference patterns as a result of 30 minutes APTES monolayer formation (blue circles) and model generated data-fitting of the same process (red lines).

It should be noted that although these parameters are unique for a given chemical reaction, solution chemistry, and temperature, the comparison with previously reported values for the silanization of APTES is difficult. It is well established that the silanization of APTES on silicon oxide (SiO_2) substrate is highly sensitive to the deposition conditions and outside environment, thus, the specific physico-chemical processes that occur during silanization vary significantly from experiments to experiment [28][29]. As shown in Fig. 16, the rate of deposition of APTES molecules onto the glass spherical tip based on the Langmuir kinetics was able to model the time profile of the spectral shift of the interference patterns during APTES monolayer formation from different bulk concentration.

The results thus far demonstrate that the fiber-coupled probe could be used in real-time binding assays to extract kinetic information of the given interactions. While the total spectral shift at equilibrium might have a relatively low sensitivity to the change in bulk concentration at higher concentration range due to the system approaching saturation, the initial slope of the spectral shift as a function of time could be used to resolve minute concentration differences. Furthermore, a more rapid assay could be achieved by utilizing only the initial rate from the real-time monitoring as oppose to employing the more conventional equilibrium level value in the point sample detection. Moreover, the spectral shift as a function of incubation time was taken from the reflected power at a single wavelength. The detection could theoretically be done with a single-wavelength light source without any needs for frequency sweeping, thus, lowering the total cost of the analysis procedure dramatically.

For the sample of known concentration, the kinetic constants Γ_{max}, k_a and k_d of the interactions can be determined. This process is an essential step in the development of new therapeutic agents as the specificity

and affinity of drugs to targeted species will greatly affect the efficacy of the treatment [10]. On the other hand, for the analysis of a certain interaction such as specific binding of antigen to its antibody pair, the concentration of the target molecules can be derived from the real-time binding data by fitting the results to known adsorption kinetics. In the case where both the transport phenomena and the reaction kinetics are well-established, such as the binding of a specific antigen to its antibody pair under a controlled flow in a microfluidic cell, the kinetic data obtained in real-time may offer a new platform of rapid CFCA [14][15]. Such analysis could make the fiber-coupled probe, given its low-cost, robust, and easy-to-fabricate nature, a promising alternatives to point-of-care diagnostics.

VI. Conclusion and Future Work

Demonstrating the mode coupling between an optical fiber and a microcavity sphere works to bring the high sensitivity of optical microcavity sensors off of the optical table and into a robust integrated microprobe [30]. The integrated microprobe design has the distinct advantage of use in vivo without the need of microfluidics or precise optical alignment of evanescent coupling, and can be implemented for sample volumes on the order of several hundred pico-liters to nano-liters, essentially a wavelength thick layer of sample surrounding the spherical tip.

The fiber-coupled microcavity probe operates on the bases of a self-reference interferometer with multiple reflections at multiple non-normal incident angles. The light source enters the probe tip via the optical fiber wedged into the finely tapered cavity inside glass spherical tip. The wave fronts scattered from the fiber tip are bent by the unique geometry of the tapered cavity, allowing the light to propagate within the spherical tip in a similar manner as a weak Q coupling of light into a spherical microcavity resonator. The multiple reflection angles allow the reflected interference signals from the probe to undergo both amplitude and phase modulation. This feature differentiates the microprobe from other optical fiber-based biosensors with similar needle-like device architecture, which only derive information from normal reflection at the flat fiber tip [31]. After multiple reflections within the glass cavity, the light eventually reenters the air cavity and couples back into the optical fiber, where it interferes with the back reflection from the flat end of the fiber. The probe model based on this principle of the effective Fabry-Perot cavity was able to describe the interference patterns of the reflected signal remarkably well. Even in the more complex cases of molecular interactions on the probe surface, modeling the layer of surface-bounded molecules as the third effective cavity with high refractive index could reproduce the seemingly counter-intuitive blue spectral shift observed during binding experiments.

The first generation pre-optimization microprobes demonstrated sensitivity in the range of 10^{-4} to 10^{-5} RIU and the 40 nm/RIU under bulk refractive index measurements. In addition, monitoring of the spectral shift during the salinization process confirms a high degree of near-field (evanescent) sensitivity to the deposition of molecules onto the probe surface as the formation of the 5 Å self-assembled APTES monolayer was detected in real-time. Performing the silanization procedure at different concentration of APTES in the solution demonstrated that kinetics of the interactions may be extracted from the real-time data. The time profile of the spectral shift was shown to reflect the binding rate of APTES molecules as the data fitted the Langmuir physico-chemical adsorption kinetics over the range of concentrations tested. In addition, utilizing the initial rate of spectral shift from the real-time monitoring could resolve much smaller concentration differences than the more conventional equilibrium data from point sample detection. Thus, the experimental results demonstrate the proof-of-concept that this fiber-coupled microcavity probe can be used for detection of specific bio-targets in the evanescence near-field zone of the glass cavity, and even has potential use in studying real-time surface interaction kinetics and perform CFCA for point-of-care diagnostics.

Although the specific wave characteristics of reflected light from the first generation prototypes varies from device to device due to the non-uniform probe geometry, the implementation of an automated fabrication platform with mechanical stages could control the size and curvature of the tapered air cavity and the glass spherical tip. Furthermore, though exhibiting sensitivity in bulk solution less than that achieved in other optical biosensors such as Surface Plasmon Resonance sensors, ring resonator sensors and interferometric sensors, which are able to detect down to 10^{-7} RIU, the data recorded thus far is from proof-of-concept hand-made microprobes that are yet to undergo optimization as far as their cavity size and geometric effects on mode coupling [12]. For example, by fabricating smaller diameter spherical tips, we will be able to increase the nm/RIU limit of detection due to a shorter effective cavity length. Similarly, implementing the controlled automated fabrication platform, we hope to optimize the geometry of the tapered air cavity and probe curvatures. This optimization could lead to enhanced mode coupling between the fiber and the spherical tip by bending the incoming wave fronts such that the reflections in the spherical tip occur at the optimal angles for maximum coupling Q-factor. In addition, the geometric variations of the tapered air cavity and probe curvature could allow for tunability between the competing effects of the reflection coefficient modulation and Goos-Hänchen phase shift for the creation of far field and near field sensors, respectively.

Acknowledgment

The authors wish to thank Anubhav Tripathi and Domenico Pacifici for their support and helpful discussion for this study. The authors are also very grateful for the guidance of Jin Ho Kim, Gustavo Fernandes, and Carlos Bledt, and the support of Center for Biomedical Engineering

at Brown University, ARL, AFOSR, CR Bard, and WCU program at Seoul National University.

REFERENCES

[1] Z. Ballard, N. Leartprapun, and J. Xu, "Fiber-coupled microcavity probe for in-vivo near-field sensing," *The Fourth International Conference on Sensor Device Technologies and Applications* (SENSORDEVICE 2013) IARIA, Aug. 2013, pp. 107-111, ISSN: 2308-3514, ISBN: 978-1-61208-297-4.

[2] M. A. Cooper, "Label-free screening of bio-molecular interactions,"*Anal. Bioanal. Chem.*, vol. 377, no. 5, pp. 834-842, 2003, doi: 10.1007/s00216-003-2111-y.

[3] S.O. Kasap, Optoelectronics and photonics, principles and practices, Prentice-Hall, pp. 1-42, 2001, ISBN: 0-201-61087-6.

[4] X. Zhang, C.R. Yonzon, M.A. Young, D.A. Stuart and R.P. Van Duyne, "Surface-enhanced Raman spectroscopy biosensors: excitation spectroscopy for optimisation of substrates fabricated by nanosphere lithography," *IEE Proc.-Nanobiotechnol.*, vol. 152, no. 6, pp. 195-206, 2005.

[5] B. Yu, A. Wang, and G. R. Pickrell, "Analysis of fiber Fabry–Pérot interferometric sensors using low-coherence light sources," *J. Lightwave Technol.*, vol. 24, no. 4, pp. 1758-1767, 2006, doi: 10.1109/JLT.2005.863336.

[6] H. N. Daghestani and B. W. Day, "Theory and applications of surface plasmon resonance, resonant mirror, resonant waveguide grating, and dual polarization interferometry biosensors," *Sensors*, vol. 10, pp. 9630-9646, 2010, doi: 10.3390/s101109630.

[7] F. Vollmer and L. Yang, "Label-free detection with high-Q microcavities: a review of biosensing mechanisms for integrated devices," *Nanophotonics*, vol. 1, pp. 267-291, 2012, doi: 10.1515/nanoph-2012-0021.

[8] T. Yoshie, L. Tang, and S. Y. Su, "Optical microcavity: sensing down to single molecules and atoms," *Sensors*, vol. 11, pp. 1972-1991, 2011, doi: 10.3390/s110201972.

[9] M. N. Velasco-Garcia, "Optical biosensors for probing at the cellular level: A review of recent progress and future prospects," *Seminars in cell & developmental biology*, vol. 20, no. 1. Academic Press, pp. 27-33, Feb. 2009, doi: 10.1016/j.semcdb.2009.01.013.

[10] Y. Fang, "Label-free optical biosensors in drug discovery," *Trends in Bio/Pharmaceutical Industry*, vol. 3, pp. 34-38, 2007.

[11] F. S. Ligler, "Perspective on optical biosensors and integrated sensor systems," *Anal. Chem.*, vol. 81, no. 2, pp. 519-526, 2009, doi: 10.1021/ac8016289.

[12] X. Fan, I. M. White, S. I. Shopova, H. Zhu, J. D. Suter, and Y. Sun, "Sensitive optical biosensors for unlabeled targets: A review," *Anal. Chim. ACTA*, vol. 620, no. 1, pp. 8-26, 2008, doi: 10.1016/j.aca.2008.05.022.

[13] C. Bee, Y. N. Abdiche, J. Pons, and A. Rajpal, "Determining the binding affinity of therapeutic monoclonal antibodies towards their native unpurified antigens in human serum," *PLoS ONE*, vol. 8, no. 11: e80501, pp. 1-13, 2013, doi: 10.1371/journal.pone.0080501.

[14] K. Sigmundsson, G. Másson, R. Rice, N. Beauchemin, and B. Öbrink, "Determination of active concentrations and association and dissociation rate constants of interacting biomolecules: an analytical solution to the theory for kinetic and mass transport limitations in biosensor technology and its experimental verification," *Biochemistry-US.*, vol. 41, no. 26, pp. 8263-8276, 2002, doi: 10.1021/bi020099h.

[15] S. Rodriguez-Mozaz, M. J. Lopez de Alda, M. Marco, and D. Barcelo, "Biosensors for environmental monitoring: A global perspective," *Talanta*, vol. 65, no. 2, pp. 291-297, 2005, doi: 10.1016/j.talanta.2004.07.006.

[16] O. R. Ranjbara, et al., "High pressure discrimination based on optical fiber microsphere cavity Fizeau interferometer," *Proc. of SPIE*, vol. *8421*, 2012, doi: 10.1117/12.966322.

[17] D. Q. Chowdhury, D. H. Leach, and R. K. Chang, "Effect of the Goos-Häinchen shift on the geometrical-optics model for spherical-cavity mode spacing," *J. Opt. Soc. Am. A*, vol. 11, no. 3, pp. 1110-1116, 1994, doi: 10.1364/JOSAA.11.001110.

[18] M. A. Cooper, "Optical biosensors in drug discovery," *Nat. Rev. Drug Discov.*, vol. 1, pp. 515-528, 2012, doi: 10.1038/nrd838.

[19] B. John, "Optical biosensors for unlabelled bio-molecules detection: future development trends," *Third National Conference on Modern Trends in Electronic Communication & Signal Processing*, 2013.

[20] A. V. Krasnoslobodtsev and S. N. Smirnov, "Effect of water on silanization of silica by trimethoxysilanes," *Langmuir*, vol. 18, no. 8, pp. 3181-3184, 2002, doi: 10.1021/la015628h.

[21] M. Zhu, M. Z. Lerum, and W. Chen, "How to prepare reproducible, homogeneous, and hydrolytically stable aminosilane-derived layers on silica,"*Langmuir*, vol. 28, no. 1, pp. 416-423, 2012, doi: 10.1021/la203638g.

[22] F. Vollmer and S. Arnold, "Whispering-gallery-mode biosensing: label-free detection down to single molecules," *Nat. Methods*, vol. 5, no. 7, pp. 591-596, 2008, doi: :10.1038/NMETH.1221.

[23] K. M. De Vos, I. Bartolozzi, P. Bienstman, R. Baets, and E. Schacht, "Optical biosensor based on silicon-on-insulator microring cavities for specific protein binding detection-art. no. 64470K," *P. Soc. Photo-Opt. Ins. IV*, vol. 6447, pp. 64470K1-64470K8, 2007, doi: 10.1117/12.698875.

[24] Y. Guo, et al., "Label-free biosensing using a photonic crystal structure in a total-internal-reflection geometry," *SPIE BiOS: Biomedical Optics*, vol. 7188, pp. 71880B–71880B12, 2009, doi: 10.1117/12.808369.

[25] M. Ritzefeld and N. Sewald, "Real-time analysis of specific protein-DNA interactions with Surface Plasmon Resonance," *J. Amino Acids*, vol. 2012, pp. 1-19, 2012, doi: 10.1155/2012/816032.

[26] E. S. Daya, A. D. Capilia, C. W. Borysenko, M. Zafaria and A. Whitty, "Determining the affinity and stoichiometry of interactions between unmodified proteins in solution using Biacore," *Anal. Biochem.*, vol. 440, no. 1, pp. 96-107, 2013, doi: 10.1016/j.ab.2013.05.012.

[27] A. Islam, M. R. Kahn and S. I. Mozumber, "Adsorption equilibrium and adsorption kinetics: a unified approach," *Chem. Enq. Technol.*, vol. 27, no. 10, pp. 1095-1098, 2004, doi: 10.1002/ceat.200402084.

[28] N. Aissaoui, L. Bergaoui,J. Landoulsi, J. F. Lambert, and S. Boujday, "Silane layers on silicon surfaces: mechanism of interaction, stability, and influence on protein adsorption," *Lamgmuir*, vol. 28, no. 1, pp. 656-665, 2012, doi: 10.1021/la2036778.

[29] E. T. Vandenberg, et al., "Structure of 3-aminopropyl triethoxy silane on silicon oxide," *J. Colloid Interf. Sci.*, vol. 147, no. 1, pp. 103-118, 1991, doi: 10.1016/0021-9797(91)90139-Y.

[30] S. Arnold, S. I. Shopova, and S. Holler, "Whispering gallery mode bio-sensor for label-free detection of single molecules: thermo-optic vs. reactive mechanism," *Opt. Express*, vol. 18, no. 1, pp. 281-287, 2010, doi: 10.1364/OE.18.000281.

[31] D. Dey, T. Godswami, "Optical Biosensors: A Revolution Towards Quantum Nanoscale Electronics Device Fabrication," *J. Biomed. Biotechnol.*, vol. 2011, pp. 1-7, 2011, doi: 10.1155/2011/348218.